

Gaussian-LIC: Photo-realistic LiDAR-Inertial-Camera SLAM with 3D Gaussian Splatting

Xiaolei Lang^{1,†}, Laijian Li^{1,†}, Hang Zhang², Feng Xiong², Mu Xu², Yong Liu¹, Xingxing Zuo^{3,*}, Jiajun Lv^{1,*}

Abstract—We present a real-time LiDAR-Inertial-Camera SLAM system with 3D Gaussian Splatting as the mapping backend. Leveraging robust pose estimates from our LiDAR-Inertial-Camera odometry, Coco-LIC, an incremental photo-realistic mapping system is proposed in this paper. We initialize 3D Gaussians from colorized LiDAR points and optimize them using differentiable rendering powered by 3D Gaussian Splatting. Meticulously designed strategies are employed to incrementally expand the Gaussian map and adaptively control its density, ensuring high-quality mapping with real-time capability. Experiments conducted in diverse scenarios demonstrate the superior performance of our method compared to existing radiance-field-based SLAM systems.

I. INTRODUCTION

Simultaneous localization and mapping (SLAM) serves as a foundational capability required for a variety of applications, such as mobile robots and mixed reality. In recent years, the radiance field representations [1–5] incorporated into SLAM for scene representation has emerged as an exciting direction within SLAM research community. The fundamental goal for radiance-field-based SLAM is to localize accurately while performing photorealistic scene reconstruction efficiently with real-time perception capability.

Many existing radiance-field-based SLAM adopt Neural Radiance Fields (NeRF) [1, 4] scene representation to generate fine-grained maps [6–15]. However, such implicit neural representations necessitate computationally intensive volumetric rendering based on strategic sampling in 3D space, undermining the real-time capability essential for SLAM applications. Recently, 3D Gaussian Splatting (3DGS) [5], a novel and promising scene representation method, has been displayed with fast rendering speed and superior visual quality. Besides, as an explicit and interpretable representation, 3DGS enables straightforward scene editing, beneficial for numerous downstream tasks. Several works have pioneered to integrate 3DGS into SLAM systems for improved rendering speed and accuracy [16–20].

However, all existing radiance-field-based SLAM systems, including both NeRF-based or 3DGS-based, are mainly tested in well-lit small-scale indoor environments and

achieve satisfying results using sequential RGB-D or RGB inputs [6–14, 16–20]. However, these methods encounter difficulties when scaling up to large-scale uncontrolled outdoor scenes characterized by challenging lighting conditions, cluttered backgrounds, and highly dynamic ego motions. In this work, we address these challenges by fusing data from multiple sensors, including a 3D LiDAR, an IMU, and a camera (referred to as LIC), to achieve robust pose estimation and generate photo-realistic maps based on 3DGS in uncontrolled outdoor scenarios.

In consideration of the aforementioned challenges, we present Gaussian-LIC, a SLAM system based on multimodal radiance fields. Gaussian-LIC integrates heterogeneous LIC measurements for robust pose tracking, and utilizes colorized LiDAR point clouds as a prior to incrementally reconstruct a precise Gaussian map in real-time, enabling rapid and high-fidelity rendering. Our contributions can be summarized as follows:

- We introduce the *first* 3DGS-based SLAM system based on LiDAR-Inertial-Camera fusion, achieving highly accurate pose tracking and photo-realistic online mapping.
- We capitalize on the sequential colored LiDAR point cloud as a feasible prior to reconstruct a Gaussian map online. A series of strategies have been meticulously designed to incrementally expand the Gaussian map and adaptively control its density to achieve high efficiency and accuracy.
- Our method undergoes extensive verification in both indoor and outdoor scenarios, showcasing state-of-the-art performance in photo-realistic mapping. It demonstrates robustness in adverse conditions, including highly dynamic motion, low illumination, and lack of geometric structures and visual textures.

II. RELATED WORK

A. NeRF-based SLAM

iMAP [6], the first NeRF-based SLAM that employs the implicit neural representation to achieve watertight online reconstruction, has pioneered a new era in SLAM. As a follow up, NICE-SLAM [7] combines MLPs with hierarchical feature grids, markedly improving the quality of scene representation and realizing outstanding performance in larger indoor environments. Further, Vox-Fusion [8] utilizes octree to dynamically expand the volumetric neural implicit map, eliminating the need for pre-allocated grids. Adopting hash-grids, tri-planes, and neural point clouds as implicit neural

¹ The authors are with the Institute of Cyber-Systems and Control, Zhejiang University, Hangzhou, China.

² The authors are with AMAP.

³ The author is with the Technical University of Munich, Munich, Germany.

[†] The co-first authors have equal contributions.

* Xingxing Zuo and Jiajun Lv are the corresponding authors, Email: xingxing.zuo@tum.de; lvjiajun314@zju.edu.cn.

representations respectively, Co-SLAM [9], ESLAM [10], and Point-SLAM [11] get enhancement in both localization and reconstruction. Unlike previous RGB-D SLAM, Orbeez-SLAM [12], NeRF-SLAM [13], and NeRF-VO [15] operate solely on monocular images. NeRF-SLAM [13] utilizes the dense depth maps estimated from dense DROID-SLAM [21] as additional information to supervise the training of Instant-NGP [4]. NeRF-VO [15] employs sparse visual odometry for achieving high-efficiency pose tracking while facilitating the training of neural scene representation with network-predicted dense depth and normal maps. It can achieve both photo-realistic image rendering and high-fidelity 3D dense mapping.

B. 3DGS-based SLAM

Compared to NeRF, which employs time-consuming ray-based volume rendering, 3DGS utilizes point-based rendering or fast rasterization, accelerating image view synthesis, while producing promising rendering quality. SplatAM [17], Gaussian-SLAM [18], and GS-SLAM [16] detailedly elucidate the significant advantages of 3DGS over existing map representations in SLAM tasks for online photo-realistic mapping, while they also indicate vanilla 3DGS for offline novel-view image synthesis should be properly tailored for efficiency-critical SLAM application. The aforementioned methods rely on RGB-D camera sensors to achieve real-time and photorealistic reconstruction performance. MonoGS [19], utilizing a single RGB sensor, introduces geometric regularization to address ambiguities in incremental reconstruction and performs well with monocular images. Meanwhile, Photo-SLAM [20] utilizes the classical visual odometry ORB-SLAM3 [22] for accurate pose estimation and reconstructs a hybrid Gaussian map with ORB features.

C. Multi-sensor Fusion

Traditional SLAM systems deploy filter-based or graph-based solvers to estimate ego motion and typically achieve more robust, more accurate, and faster localization performance compared to neural methods, especially when integrating multimodal sensors. Among them, LiDAR-Inertial-Camera SLAM systems might be the most versatile, with complementary sensors providing high-rate motion compensation, precise geometry structure, and rich texture information [23–29]. Nevertheless, their primary focus lies in geometric mapping, resulting in geometrically precise yet visually simple representations of the scene. DrivingGaussian [30], StreetGaussian [31], and LIV-GaussMap [32] perform photorealistic reconstructions based on LiDAR-camera fusion, but all of them are offline methods. On the contrary, our proposed system not only relies on multi-sensor fusion to deliver robust, real-time, and accurate pose estimation but also realizes photorealistic online mapping with LiDAR-camera fusion. Compared to RGB-D camera or RGB camera only systems, our method achieves superior performance in tracking and mapping, capable of adapting to more general scenarios, both indoors and outdoors.

III. METHODOLOGY

We provide an overview of the proposed LIC-SLAM system in Fig. 1. We aim to simultaneously estimate pose and perform photorealistic scene reconstruction based on LiDAR-Inertial-Camera fusion.

A. 3D Gaussian Splatting Representation

In order to produce a richly detailed dense map for fast and high-quality rendering, we represent the scene as a collection of anisotropic 3D Gaussians, each of which contains position $\boldsymbol{\mu} \in \mathbb{R}^3$ in the world coordinate, scale $\mathbf{S} \in \mathbb{R}^3$, rotation $\mathbf{R} \in \mathbb{R}^{3 \times 3}$, opacity $o \in \mathbb{R}$, and one-degree spherical harmonics $\mathbf{SH} \in \mathbb{R}^{12}$ capturing the view-dependent appearance of the scene. Representing the Gaussian’s ellipsoidal shape, the covariance of each Gaussian is parameterized as:

$$\boldsymbol{\Sigma} = \mathbf{R}\mathbf{S}\mathbf{S}^T\mathbf{R}^T. \quad (1)$$

Given the camera pose ${}^C_W\mathbf{T} = \{{}^C_W\mathbf{R}, {}^C_W\mathbf{p}_W\}$ which transforms the point ${}^W\mathbf{p}$ in the world frame $\{W\}$ into the camera frame $\{C\}$, we can splat a 3D Gaussian $\mathcal{N}(\boldsymbol{\mu}, \boldsymbol{\Sigma})$ onto the image screen and get a 2D Gaussian $\mathcal{N}(\boldsymbol{\mu}', \boldsymbol{\Sigma}')$:

$$\boldsymbol{\mu}' = \pi_c \left(\frac{\hat{\boldsymbol{\mu}}}{\mathbf{e}_3^\top \hat{\boldsymbol{\mu}}} \right), \quad \hat{\boldsymbol{\mu}} = {}^C_W\mathbf{R} \boldsymbol{\mu} + {}^C_W\mathbf{p}_W, \quad (2)$$

$$\boldsymbol{\Sigma}' = [\mathbf{J} {}^C_W\mathbf{R} \boldsymbol{\Sigma} {}^C_W\mathbf{R}^T \mathbf{J}^T]_{2 \times 2}, \quad (3)$$

where \mathbf{e}_i is a 3×1 vector with its i -th element to be 1 and the other elements to be 0. $\pi_c(\cdot)$ denotes the projection operation which transforms a point on the normalized image plane to a pixel. \mathbf{J} is the Jacobian of the affine approximation of the projective transformation and $[\cdot]_{2 \times 2}$ skips the third row and column to acquire a 2×2 matrix. The projected 2D Gaussian affects the pixel $\boldsymbol{\rho} = [u \ v]^\top$ by the opacity-weighted equation:

$$\alpha = o \exp \left(-\frac{1}{2}(\boldsymbol{\mu}' - \boldsymbol{\rho})^T (\boldsymbol{\Sigma}')^{-1} (\boldsymbol{\mu}' - \boldsymbol{\rho}) \right) \quad (4)$$

Sorting the Gaussians in depth order, the color of the pixel $\boldsymbol{\rho}$ can be efficiently rendered via front-to-back α -blending:

$$\mathbf{C}(\boldsymbol{\rho}) = \sum_{i=1}^n \mathbf{c}_i \alpha_i \prod_{j=1}^{i-1} (1 - \alpha_j), \quad (5)$$

where \mathbf{c} denotes the RGB color of the Gaussian computed from \mathbf{SH} .

Similarly, we also render a silhouette image to determine whether a pixel has contained sufficient information from the Gaussian map, as GS-SLAM [16] and SplatAM [17] do:

$$\mathbf{V}(\boldsymbol{\rho}) = \sum_{i=1}^n \alpha_i \prod_{j=1}^{i-1} (1 - \alpha_j), \quad (6)$$

B. LiDAR-Inertial-Camera Odometry

We adopt our previous work, Coco-LIC [29], a continuous-time tightly-coupled LiDAR-Inertial-Camera odometry system, as the tracking front-end. By integrating three complementary sensors, we attain robust, real-time, and highly accurate pose estimation, facilitating the entire SLAM system.

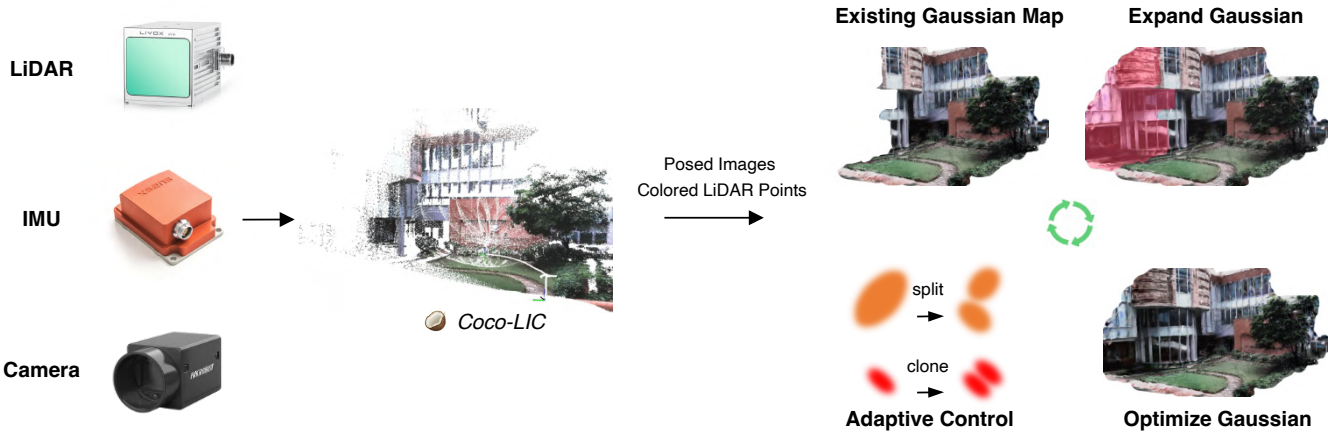


Fig. 1: The pipeline of our novel multimodal radiance-field-based SLAM system with a fusion of LiDAR, IMU, and camera measurements. The pose tracking module is our previous work Coco-LIC [29], which delivers robust and accurate poses based on continuous-time trajectory optimization. In parallel, with the pose tracking results and the by-product colored LiDAR point clouds, our proposed mapping thread incrementally reconstructs a Gaussian map in real time for photo-realistic rendering, empowered by our carefully crafted expansion and adaptive density control strategies.

Every time the LiDAR-Inertial-Camera data in the latest Δt (0.1 in this paper) seconds is accumulated, we efficiently optimize the trajectory segment in the time interval based on a factor graph, with scan-to-map LiDAR factors, frame-to-map visual factors, IMU factors, and bias factors. Note that we only make use of the latest image for the optimization in a time interval.

3DGS reconstruction needs to be bootstrapped by a set of 3D points. In contrast to SFM points used in the vanilla 3DGS [5], LiDAR points provide more precise geometric priors [30–32]. Additionally, it is worth mentioning that LiDAR points are handy and readily accessible in our system. We maintain a global LiDAR map stored in voxels with a resolution of 0.1 m . After optimizing the trajectory in the current time interval, for efficiency, only a quarter of the LiDAR points in this period are transformed into the world coordinate and appended to the voxels, ensuring that the distance between LiDAR points in each voxel should be larger than 0.05 m , so as to reduce redundancy. For successfully appended LiDAR points, we project them onto the latest image and color them by querying the pixel values. Subsequently, they are sent to the mapping thread, together with the latest image with the estimated camera pose, regarded as a frame.

C. 3DGS-based Photorealistic Mapping

With the estimated camera poses, undistorted images, and colored LiDAR points continuously inputted, the mapping module progressively builds and optimizes the Gaussian map. Different from the vanilla offline method [5], modifications are needed in the incremental mode.

1) *Initialization*: To bootstrap our SLAM system, all LiDAR points received in the first time interval are utilized to create new Gaussians. To be specific, for each LiDAR point, we initialize a new Gaussian centered at its position with the

zeroth degree of \mathbf{SH} filled with its RGB color, opacity set to be 0.1, and rotation set to be the identity matrix. To mitigate the aliasing artifacts, we assign smaller scales for the closer Gaussians, while larger scales for those far away from the image plane [17, 33]:

$$\mathbf{S} = \frac{2d}{f}\mathbf{e}, \quad (7)$$

where \mathbf{e} is a 3×1 vector filled with ones. d denotes the depth of the LiDAR point in the image frame and f is the focal length of the camera. The Gaussians will have a two-pixel radius when projected onto the image.

2) *Expansion*: Every frame received after the first frame usually captures the geometry and appearance of the newly observed areas. However, LiDAR points from different frames may contain duplicate or extremely similar information. To avoid redundancy, we first render a silhouette image \mathbf{V} from the current image view according to Eq.(6) and generate a mask \mathbf{M} to select pixels that are not reliable from the current Gaussian map and tend to observe new areas:

$$\mathbf{M} = \mathbf{V} < 0.99. \quad (8)$$

Only LiDAR points which can be projected onto the selected pixels are utilized to initialize new Gaussians in the same manner as Sec. III-C.1, to expand the Gaussian map.

3) *Optimization*: Given images with estimated camera poses from Coco-LIC, the Gaussian map can be continually optimized. However, using all received images to perform optimization is computationally infeasible for our online incremental mapping system, and thus we take every fifth frame as a keyframe. To maintain bounded computation complexity for efficiency, we select K active keyframes to optimize the Gaussian map, including the first and the last one, as well as other random $K - 2$ ones, avoiding the catastrophic forgetting problem and keeping the geometric

consistency of the global map. We randomly shuffle the selected K keyframes and iterate through each of them to optimize the map by minimizing re-rendering loss:

$$\mathcal{L} = (1 - \lambda) \|\mathbf{I} - \bar{\mathbf{I}}\|_1 + \lambda \mathcal{L}_{D-SSIM}, \quad (9)$$

where $\bar{\mathbf{I}}$ and \mathbf{I} are the observed image and the image rendered by Eq.(5), respectively. \mathcal{L}_{D-SSIM} is a D-SSIM term.

4) *Adaptive Control*: Though providing accurate geometric priors, the LiDAR scans could not cover the whole scene, especially in the unbounded outdoor environments. Hence, compared to previous works designed for indoor scenes with RGB-D sensors, it would be more necessary here to execute adaptive control to densify the Gaussian map over unit volume. However, naive adoption of the adaptive control strategy in [5] leads to incorrect densification.

The original strategy handles Gaussians with larger gradients at a constant interval, while in the incremental mode, recently added Gaussians can be mistakenly cloned or split because they often have larger gradients due to not having converged yet. To this end, we classify the existing Gaussians into stable and unstable categories and densify only the stable Gaussians. Concretely, we keep track of optimization iterations for each Gaussian and accumulate the gradients for those who have been optimized more than N times. Gaussians accumulating gradients over M times will be cloned or split if the average gradient exceeds τ , or removed if the opacity lowers than ϵ . Once densified, the accumulated information of operated *stable* Gaussians will be reset.

D. Implementation Details

Our SLAM method Gaussian-LIC consists of two parallel threads, a tracking module and a mapping module, facilitating the exchange of the data based on ROS. Both modules are implemented in C++. The mapping module is based on the LibTorch framework¹, incorporating CUDA for Gaussian rasterization. Gaussian-LIC is run on a desktop PC with an NVIDIA RTX 3090 24 GB GPU, a 3.2GHz Intel Core i7-8700 CPU, and 32 GB RAM. We set the loss weighting λ to 0.2 and the number K of selected keyframes to 100. As for adaptive control, we set N to 500, M to 100, τ to 0.00015, and ϵ to 0.005. The learning rate for the mean positions of Gaussians is not decayed and is set to 0.00016. Experiments in all tested scenarios share the same hyperparameters for fair comparison.

IV. EXPERIMENTS

To verify the performance of our proposed system, we conduct extensive experiments on real-world indoor and outdoor datasets, evaluating the performance in both tracking and photorealistic mapping. Also, we provide runtime analysis and justify the effectiveness of our system via ablation study.

TABLE I: **Pose tracking performance of radiance-field-based SLAM methods on the R3LIVE dataset, FAST-LIVO dataset, and BotanicGarden dataset.** On the first two datasets, we use the start-to-end drift error as the evaluation metric, where \checkmark , \circ , and \times denote successfully returning to the origin, approaching the origin, and very large drift, respectively. As for the BotanicGarden dataset, the RMSE of APE results are shown.

	NeRF-SLAM [13]	MonoGS [19]	Gaussian-LIC
<i>hku_campus_seq_00</i>	\circ	\times	\checkmark
<i>degenerate_seq_00</i>	\circ	\times	\checkmark
<i>hku2</i>	\checkmark	\times	\checkmark
<i>LiDAR_Degenerate</i>	\checkmark	\circ	\checkmark
<i>Visual_Challenge</i>	\times	\times	\checkmark
<i>1018-00</i>	0.378	9.942	0.252
<i>1018-09</i>	1.629	9.146	0.461

A. Datasets

We carry out experiments on three public LiDAR-Inertial-Camera datasets, including the R3LIVE [26] dataset, the FAST-LIVO [27] dataset, and the BotanicGarden [34] dataset. The first two datasets are collected within the campuses of HKU and HKUST using a handheld device equipped with a Livox Avia² LiDAR at 10Hz and its built-in IMU at 200Hz, and a 15Hz RGB camera. They comprise both indoor and outdoor sequences. Notably, some sequences feature degeneration cases for SLAM, which provides a test bed for the robustness of various methods. Note that in super large-scale scenarios, the drift of the odometry will severely affect the mapping thread, and numerous Gaussians can lead to GPU overflow. Though mapping solutions at a large scale exist, they are beyond the scope of this paper. In our experiments, we only select sequences with the length of the trajectory under 200 m , including *hku_campus_seq_00*, *degenerate_seq_00*, and *hkust_campus_02* (top 150 seconds only) from the R3LIVE dataset, as well as *hku2*, *LiDAR_Degenerate*, and *Visual_Challenge* from the FAST-LIVO dataset. The BotanicGarden dataset is collected by a wheeled robot traversing through a luxuriant botanic garden. Analogous to the first two datasets, measurements from Livox Avia and the internal IMU are also provided with stereo RGB images but we only use the left images. We select *1018-00* and *1018-09* for evaluation, with the trajectory lengths of 115 m and 157 m , respectively. Table II contains basic information about each sequence.

B. Baselines

We compare our multimodal radiance-field-based SLAM system with state-of-the-art RGB systems, including NeRF-based method NeRF-SLAM [13] and 3DGS-based method MonoGS [19]. It should be noted that when stepping into unbounded outdoor scenarios, depth from RGB-D cameras with a short sensing range is usually not reliable, therefore RGB-D radiance field methods are excluded in our experiments. In the experiments, all methods use images with a resolution of 640×512 on the R3LIVE dataset and the FAST-LIVO dataset, and 960×600 on the BotanicGarden dataset.

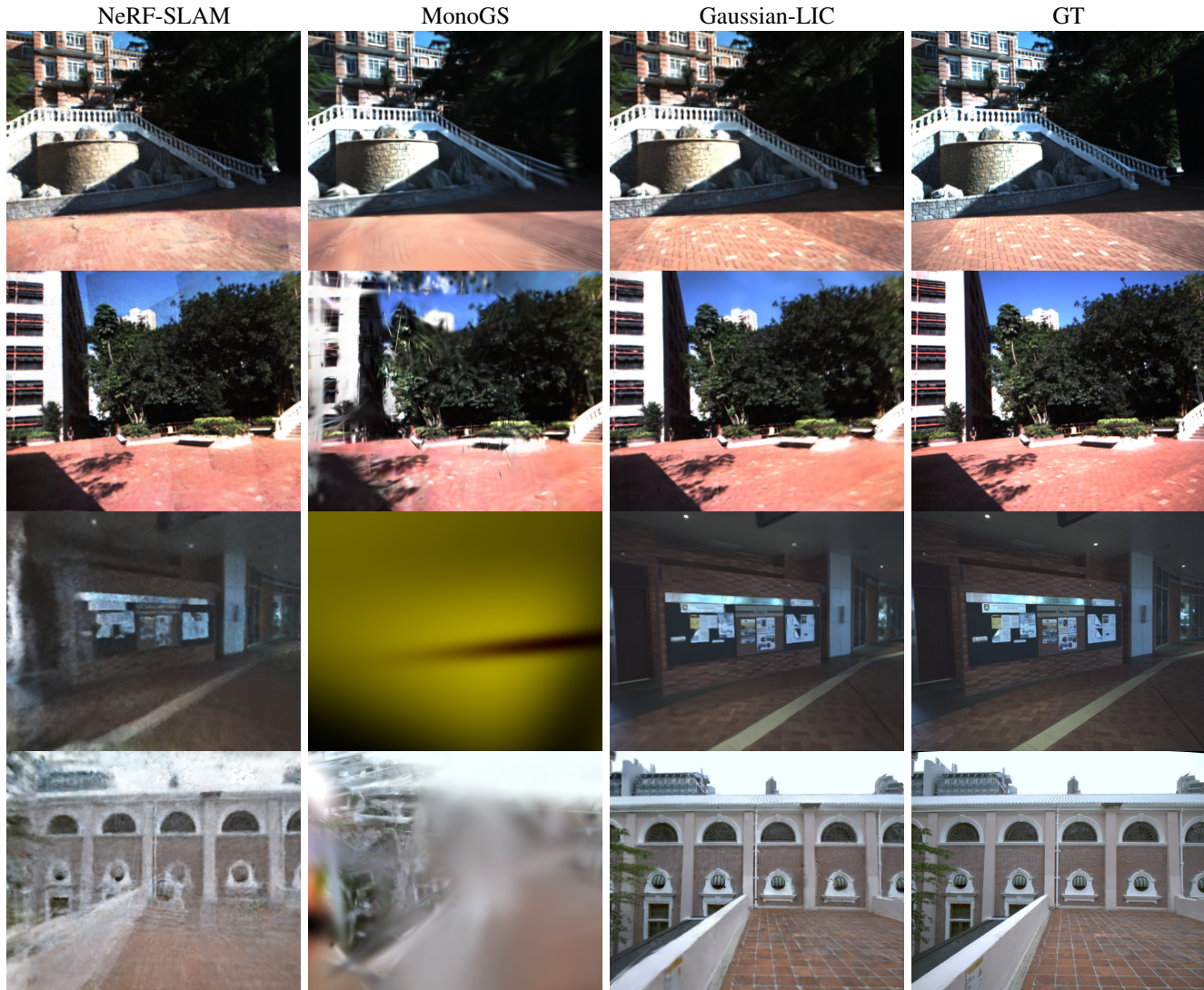
¹<https://github.com/pierotofy/OpenSplat>

²<https://www.livoxtech.com/avia>

TABLE II: **Quantitative rendering performance comparison of radiance-field-based SLAM methods on the R3LIVE dataset, FAST-LIVO dataset, and BotanicGarden dataset.** The best results are marked in bold. I means indoor and O means outdoor.

	Sensor Degeneration	Scenarios	Length (m)	NeRF-SLAM [13]			MonoGS [19]			Gaussian-LIC		
				PSNR \uparrow	SSIM \uparrow	LPIPS \downarrow	PSNR \uparrow	SSIM \uparrow	LPIPS \downarrow	PSNR \uparrow	SSIM \uparrow	LPIPS \downarrow
<i>hku_campus_seq_00</i>	-	I, O	191	19.14	0.535	0.440	14.53	0.462	0.751	24.90	0.795	0.240
<i>hkust_campus_02</i>	-	O	118	16.46	0.507	0.403	14.89	0.475	0.661	20.61	0.701	0.245
<i>degenerate_seq_00</i>	LiDAR	O	53	18.58	0.554	0.344	16.06	0.593	0.532	22.62	0.794	0.205
<i>hku2</i>	-	O	59	25.23	0.621	0.283	21.42	0.559	0.652	28.82	0.794	0.196
<i>LiDAR_Degenerate</i>	LiDAR	I	38	27.47	0.722	0.252	24.91	0.728	0.664	29.51	0.821	0.232
<i>Visual_Challenge</i>	Camera	I, O	78	19.01	0.533	0.492	15.23	0.572	0.750	23.24	0.791	0.244
<i>1018-00</i>	-	O	115	15.17	0.352	0.523	14.82	0.342	0.641	18.65	0.596	0.387
<i>1018-09</i>	-	O	157	12.15	0.234	0.620	15.13	0.343	0.632	18.60	0.546	0.437

Fig. 2: **Qualitative rendering performance comparison of radiance-field-based SLAM methods**, in the *degenerate_seq_00*, *hku_campus_seq_00*, and *Visual_Challenge* sequences.



C. Tracking Performance

The ground truth is not provided in the R3LIVE dataset and the FAST-LIVO dataset, but the sensor rig starts and ends at the same position in all evaluated sequences except *hkust_campus_02*. Due to the inability of the two monocular methods to compute the start-to-end error with absolute scale, we observe the estimated trajectory of each method

and categorize them into successfully returning to the origin, approaching the origin, and large drift. Nonetheless, the BotanicGarden dataset offers high-quality ground truth poses, thus we can quantitatively test all methods via the RMSE of APE. Table I displays the tracking performance. Employing a really powerful neural-based visual odometry, Droid-SLAM [21], as the tracking front-end, NeRF-SLAM achieves great pose estimation in well-lit indoor scenes,



Fig. 3: The Gaussian map of the *hku_campus_seq_00* sequence reconstructed by our Gaussian-LIC. The Gaussian map is visualized by SuperSplat³.

such as *LiDAR_Degenerate*. However, it yields relatively poor results under outdoor lighting variations or when the camera moves drastically, such as in *degenerate_seq_00* and *Visual_Challenge*, so does MonoGS, which performs map-centric pose tracking via backpropagating photometric loss. Inferior pose estimation of MonoGS leads to an erroneous update of the Gaussian map, which in turn affects tracking. In contrast, based on traditional odometry method, Gaussian-LIC attains the best tracking performance by additionally tightly coupling LiDAR and IMU, regardless of scenarios.

D. Rendering Performance

Quantitative metrics in terms of Peak Signal to Noise Ratio (PSNR), Structural Similarity (SSIM), and Learned Perceptual Image Patch Similarity (LPIPS) are adopted to analyze the performance of photorealistic mapping on the input views. Table II shows that Gaussian-LIC consistently generates the best performance in all metrics on each sequence. Due to low-quality pose estimation, MonoGS fails to produce a desirable Gaussian map. Its way of initializing new Gaussians by a constant value with random noise at the beginning and subsequently by the median depth of the rendered image during tracking, seems inappropriate for large-scale outdoor scenes. NeRF-SLAM displays slightly better results but renders full-resolution images from neural implicit maps at a low speed with artifacts. Contrarily, Gaussian-LIC harnesses accurate geometric priors from LiDAR point cloud to incrementally build the Gaussian map as illustrated in Fig. 3, resulting in fast rendering of high-fidelity images, as shown in Fig. 2.

E. Runtime Analysis

We evaluate the time consumption for the proposed method in the *hku_campus_seq_00* sequence. We optimize the Gaussian map only when receiving a keyframe and select 100 keyframes for each iteration. Our method is able to complete the optimization of 100 keyframes within 1 second with an image resolution of 640×512 .

³<https://playcanvas.com/supersplat/editor>

TABLE III: **Ablation study on *hku2***. We analyze the usefulness of silhouette images and incremental adaptive control to our system.

	PSNR \uparrow	SSIM \uparrow	LPIPS \downarrow	Number
w/o silhouette image	28.80	0.795	0.194	269w
w/o adaptive control	28.65	0.789	0.205	127w
w naive adaptive control	25.78	0.772	0.209	154w
w incremental adaptive control	28.82	0.794	0.196	136w

F. Abalation Study

1) *Silhouette Image*: As illustrated in Sec. III-C.2, we utilize silhouette images to reduce redundant LiDAR points. Table III shows that if we do not employ the silhouette mask, the rendering performance barely changes, but the number of ultimate Gaussians significantly increases. Excessive repetitive LiDAR points nearly double the optimization time.

2) *Adaptive Control*: Naive employment of the original adaptive control leads to incorrect adjustment of the density, and modifications are needed for the incremental mode, as discussed in Sec. III-C.4. From Table III, it can be seen that the none of or naive adaptive control will lead to a decline in rendering quality, while the improvement can be achieved by adopting the proposed incremental strategy.

G. Discussion

Although our multi-sensor-based system outperforms state-of-the-art radiance-field-based SLAM, it has limitations and can be further improved. On the one hand, we have tried to abandon redundant LiDAR points, but excessive Gaussians are still contained in the map. Utilizing masking strategies like [35] might be useful for the removal of non-essential Gaussians. Also, we currently just run our method with solid-state LiDARs and various LiDARs will be supported later. On the other hand, the auto-exposure and motion blur of the cameras always occur, compromising the visual quality of photorealistic mapping. We will attempt to address this issue in the future.

V. CONCLUSIONS

This paper presents Gaussian-LIC, a novel LiDAR-Inertial-Camera radiance-field-based SLAM system. Based on multimodal sensors, the method accomplishes the dual feat of highly accurate tracking and photorealistic online reconstruction with 3D Gaussian Splatting. Colored LiDAR points in the world coordinate, produced by the efficient LiDAR-Inertial-Camera odometry, are used as good priors to aid the progressive establishment of the Gaussian map, where we devise a series of strategies for the incremental mode. Extensive real-world experiments demonstrate that our method outperforms state-of-the-art radiance-field-based SLAM regarding photo-realistic mapping, and ours has significantly better generalization capability in both indoor and outdoor scenarios.

REFERENCES

- [1] B. Mildenhall, P. P. Srinivasan, M. Tancik, J. T. Barron, R. Ramamoorthi, and R. Ng. "Nerf: Representing scenes as neural radiance fields for view synthesis". In: *Communications of the ACM* 65.1 (2021), pp. 99–106.

- [2] J. T. Barron, B. Mildenhall, D. Verbin, P. P. Srinivasan, and P. Hedman. "Mip-nerf 360: Unbounded anti-aliased neural radiance fields". In: *Proceedings of the IEEE/CVF Conference on Computer Vision and Pattern Recognition*. 2022, pp. 5470–5479.
- [3] S. Fridovich-Keil, A. Yu, M. Tancik, Q. Chen, B. Recht, and A. Kanazawa. "Plenoxels: Radiance fields without neural networks". In: *Proceedings of the IEEE/CVF Conference on Computer Vision and Pattern Recognition*. 2022, pp. 5501–5510.
- [4] T. Müller, A. Evans, C. Schied, and A. Keller. "Instant neural graphics primitives with a multiresolution hash encoding". In: *ACM Transactions on Graphics (ToG)* 41.4 (2022), pp. 1–15.
- [5] B. Kerbl, G. Kopanas, T. Leimkühler, and G. Drettakis. "3D Gaussian Splatting for Real-Time Radiance Field Rendering". In: *ACM Transactions on Graphics* 42.4 (2023).
- [6] E. Sucar, S. Liu, J. Ortiz, and A. J. Davison. "iMAP: Implicit mapping and positioning in real-time". In: *Proceedings of the IEEE/CVF International Conference on Computer Vision*. 2021, pp. 6229–6238.
- [7] Z. Zhu, S. Peng, V. Larsson, W. Xu, H. Bao, Z. Cui, M. R. Oswald, and M. Pollefeys. "Nice-slam: Neural implicit scalable encoding for slam". In: *Proceedings of the IEEE/CVF Conference on Computer Vision and Pattern Recognition*. 2022, pp. 12786–12796.
- [8] X. Yang, H. Li, H. Zhai, Y. Ming, Y. Liu, and G. Zhang. "Vox-Fusion: Dense tracking and mapping with voxel-based neural implicit representation". In: *2022 IEEE International Symposium on Mixed and Augmented Reality (ISMAR)*. IEEE. 2022, pp. 499–507.
- [9] H. Wang, J. Wang, and L. Agapito. "Co-SLAM: Joint Coordinate and Sparse Parametric Encodings for Neural Real-Time SLAM". In: *Proceedings of the IEEE/CVF Conference on Computer Vision and Pattern Recognition*. 2023, pp. 13293–13302.
- [10] M. M. Johari, C. Carta, and F. Fleuret. "Eslam: Efficient dense slam system based on hybrid representation of signed distance fields". In: *Proceedings of the IEEE/CVF Conference on Computer Vision and Pattern Recognition*. 2023, pp. 17408–17419.
- [11] E. Sandström, Y. Li, L. Van Gool, and M. R. Oswald. "Point-slam: Dense neural point cloud-based slam". In: *Proceedings of the IEEE/CVF International Conference on Computer Vision*. 2023, pp. 18433–18444.
- [12] C.-M. Chung, Y.-C. Tseng, Y.-C. Hsu, X.-Q. Shi, Y.-H. Hua, J.-F. Yeh, W.-C. Chen, Y.-T. Chen, and W. H. Hsu. "Orbeez-slam: A real-time monocular visual slam with orb features and nerf-realized mapping". In: *2023 IEEE International Conference on Robotics and Automation (ICRA)*. IEEE. 2023, pp. 9400–9406.
- [13] A. Rosinol, J. J. Leonard, and L. Carlone. "Nerf-slam: Real-time dense monocular slam with neural radiance fields". In: *2023 IEEE/RSJ International Conference on Intelligent Robots and Systems (IROS)*. IEEE. 2023, pp. 3437–3444.
- [14] Y. Zhang, F. Tosi, S. Mattoccia, and M. Poggi. "Go-slam: Global optimization for consistent 3d instant reconstruction". In: *Proceedings of the IEEE/CVF International Conference on Computer Vision*. 2023, pp. 3727–3737.
- [15] J. Naumann, B. Xu, S. Leutenegger, and X. Zuo. "NeRF-VO: Real-Time Sparse Visual Odometry with Neural Radiance Fields". In: *arXiv preprint arXiv:2312.13471* (2023).
- [16] C. Yan, D. Qu, D. Wang, D. Xu, Z. Wang, B. Zhao, and X. Li. "Gs-slam: Dense visual slam with 3d gaussian splatting". In: *arXiv preprint arXiv:2311.11700* (2023).
- [17] N. Keetha, J. Karhade, K. M. Jatavallabhula, G. Yang, S. Scherer, D. Ramanan, and J. Luiten. "Splatam: Splat, track & map 3d gaussians for dense rgb-d slam". In: *arXiv preprint arXiv:2312.02126* (2023).
- [18] V. Yugay, Y. Li, T. Gevers, and M. R. Oswald. "Gaussian-slam: Photo-realistic dense slam with gaussian splatting". In: *arXiv preprint arXiv:2312.10070* (2023).
- [19] H. Matsuki, R. Murai, P. H. J. Kelly, and A. J. Davison. "Gaussian Splatting SLAM". In: *Proceedings of the IEEE/CVF Conference on Computer Vision and Pattern Recognition*. 2024.
- [20] H. Huang, L. Li, H. Cheng, and S.-K. Yeung. "Photo-slam: Real-time simultaneous localization and photorealistic mapping for monocular, stereo, and rgb-d cameras". In: *arXiv preprint arXiv:2311.16728* (2023).
- [21] Z. Teed and J. Deng. "Droid-slam: Deep visual slam for monocular, stereo, and rgb-d cameras". In: *Advances in neural information processing systems* 34 (2021), pp. 16558–16569.
- [22] C. Campos, R. Elvira, J. J. G. Rodríguez, J. M. Montiel, and J. D. Tardós. "Orb-slam3: An accurate open-source library for visual, visual-inertial, and multimap slam". In: *IEEE Transactions on Robotics* 37.6 (2021), pp. 1874–1890.
- [23] X. Zuo, P. Geneva, W. Lee, Y. Liu, and G. Huang. "Lic-fusion: Lidar-inertial-camera odometry". In: *2019 IEEE/RSJ International Conference on Intelligent Robots and Systems (IROS)*. IEEE. 2019, pp. 5848–5854.
- [24] X. Zuo, Y. Yang, P. Geneva, J. Lv, Y. Liu, G. Huang, and M. Pollefeys. "Lic-fusion 2.0: Lidar-inertial-camera odometry with sliding-window plane-feature tracking". In: *2020 IEEE/RSJ International Conference on Intelligent Robots and Systems (IROS)*. IEEE. 2020, pp. 5112–5119.
- [25] T. Shan, B. Englot, C. Ratti, and D. Rus. "Lvi-sam: Tightly-coupled lidar-visual-inertial odometry via smoothing and mapping". In: *2021 IEEE international conference on robotics and automation (ICRA)*. IEEE. 2021, pp. 5692–5698.
- [26] J. Lin and F. Zhang. "R 3 LIVE: A Robust, Real-time, RGB-colored, LiDAR-Inertial-Visual tightly-coupled state Estimation and mapping package". In: *2022 International Conference on Robotics and Automation (ICRA)*. IEEE. 2022, pp. 10672–10678.
- [27] C. Zheng, Q. Zhu, W. Xu, X. Liu, Q. Guo, and F. Zhang. "FAST-LIVO: Fast and tightly-coupled sparse-direct LiDAR-inertial-visual odometry". In: *2022 IEEE/RSJ International Conference on Intelligent Robots and Systems (IROS)*. IEEE. 2022, pp. 4003–4009.
- [28] J. Lv, X. Lang, J. Xu, M. Wang, Y. Liu, and X. Zuo. "Continuous-Time Fixed-Lag Smoothing for LiDAR-Inertial-Camera SLAM". In: *IEEE/ASME Transactions on Mechatronics* (2023).
- [29] X. Lang, C. Chen, K. Tang, Y. Ma, J. Lv, Y. Liu, and X. Zuo. "Coco-LIC: continuous-time tightly-coupled LiDAR-inertial-camera odometry using non-uniform B-spline". In: *IEEE Robotics and Automation Letters* (2023).
- [30] X. Zhou, Z. Lin, X. Shan, Y. Wang, D. Sun, and M.-H. Yang. "Driving-gaussian: Composite gaussian splatting for surrounding dynamic autonomous driving scenes". In: *arXiv preprint arXiv:2312.07920* (2023).
- [31] Y. Yan, H. Lin, C. Zhou, W. Wang, H. Sun, K. Zhan, X. Lang, X. Zhou, and S. Peng. "Street gaussians for modeling dynamic urban scenes". In: *arXiv preprint arXiv:2401.01339* (2024).
- [32] S. Hong, J. He, X. Zheng, H. Wang, H. Fang, K. Liu, C. Zheng, and S. Shen. "LIV-GaussMap: LiDAR-Inertial-Visual Fusion for Real-time 3D Radiance Field Map Rendering". In: *arXiv preprint arXiv:2401.14857* (2024).
- [33] Z. Yan, W. F. Low, Y. Chen, and G. H. Lee. "Multi-scale 3d gaussian splatting for anti-aliased rendering". In: *arXiv preprint arXiv:2311.17089* (2023).
- [34] Y. Liu, Y. Fu, M. Qin, Y. Xu, B. Xu, F. Chen, B. Goossens, P. Z. Sun, H. Yu, C. Liu, L. Chen, W. Tao, and H. Zhao. "BotanicGarden: A High-Quality Dataset for Robot Navigation in Unstructured Natural Environments". In: *IEEE Robotics and Automation Letters* 9.3 (2024), pp. 2798–2805.
- [35] J. C. Lee, D. Rho, X. Sun, J. H. Ko, and E. Park. "Compact 3d gaussian representation for radiance field". In: *arXiv preprint arXiv:2311.13681* (2023).